Turbidity current flow over an erodible obstacle and phases of sediment wave generation

Moshe Strauss[1,2] and Michael E. Glinsky[2,3,4]

Received 24 August 2011; revised 21 March 2012; accepted 20 April 2012; published 7 June 2012.

[1] We study the flow of particle-laden turbidity currents down a slope and over an obstacle. A high-resolution 2-D computer simulation model is used, based on the Navier-Stokes equations. It includes poly-disperse particle grain sizes in the current and substrate. Particular attention is paid to the erosion and deposition of the substrate particles, including application of an active layer model. Multiple flows are modeled from a lock release that can show the development of sediment waves (SW). These are stream-wise waves that are triggered by the increasing slope on the downstream side of the obstacle. The initial obstacle is completely erased by the resuspension after a few flows leading to self consistent and self generated SW that are weakly dependant on the initial obstacle. The growth of these waves is directly related to the turbidity current being self sustaining, that is, the net erosion is more than the net deposition. Four system parameters are found to influence the SW growth: (1) slope, (2) current lock height, (3) grain lock concentration, and (4) particle diameters. Three phases are discovered for the system: (1) "no SW," (2) "SW buildup," and (3) "SW growth". The second phase consists of a soliton-like SW structure with a preserved shape. The phase diagram of the system is defined by isolating regions divided by critical slope angles as functions of current lock height, grain lock concentration, and particle diameters.

Citation: Strauss, M., and M. E. Glinsky (2012), Turbidity current flow over an erodible obstacle and phases of sediment wave generation, *J. Geophys. Res.*, *117*, C06007, doi:10.1029/2011JC007539.

1. Introduction

[2] Turbidity currents can trigger a variety of topographical behaviors by erosion and deposition over the seafloor, such as sediment waves (SW). These currents are particle laden and gravity driven, where the particles are suspended by fluid turbulence [*Meiburg and Kneller*, 2010]. When the bottom slope is steep enough, the current can propagate in a self-sustained mode with increasing mass and high velocity [*Parker et al.*, 1986; *Blanchette et al.*, 2005; *Sequeiros et al.*, 2009; *Pantin and Franklin*, 2009].

[3] Migrating SW generated by erosive turbidity currents have been reported in a variety of marine settings which include splays from submarine levees and submarine fans [*Wynn et al.*, 2000; *Wynn and Stow*, 2002]. The timescale of SW formation can be thousands of years and include a sequence of many turbidity currents. Typical SW wavelengths are in the range of 100 m to 5 km, and heights are in the range of 5 m to 100 m. A series of turbidity currents flowing across a rough sea can form a field of SW that migrates upstream [*Kubo and Nakajima*, 2002; *Lee et al.*, 2002]. A relation, $\lambda = 2\pi h$ was found between the SW wavelength, λ, and the turbidity current height, h, that is in agreement with observation for typical h = 60 m and λ = 380 m [*Normark et al.*, 1980; *Wynn and Stow*, 2002].

[4] The traditional explanation of the mechanism for generating a train of up-streaming SW is based on a sequence of turbidity currents flowing over an erodible bed. A supercritical flow, where the kinetic energy of the flow is larger than the potential energy (Froude number larger than one), is considered a favorable condition for the SW formation. An obstacle on the slope induces an erosion on the downstream side of the obstacle leading to a subsequent decrease in slope and to the formation of the next obstacle. This establishes a train of downstream crests in the waveform. The upstream migration of the waveform results from the preferential deposition of sediment on the upslope and the preferential erosion on the downslope. The generation of downstream undulations and the upstream migration by deposition and erosion can generate an extensive SW field. This mechanism of generating SW is similar to the generation of transportational cyclic steps [*Parker and Izumi*, 2000; *Taki and Parker*, 2005; *Sun and Parker*, 2005]. Each cyclic step is bounded by a hydraulic jump and the resulting deposition and erosion causes the waves to migrate upstream.

[1]Department of Physics, Nuclear Research Center, Negev, Beer Sheba, Israel.
[2]Earth Science and Resource Engineering Division, CSIRO, Kensington, Western Australia, Australia.
[3]School of Physics, University of Western Australia, Crawley, Western Australia, Australia.
[4]Now at ION Geophysical Inc., Houston, Texas, USA.

Corresponding author: M. E. Glinsky, ION Geophysical Inc., 2105 CityWest Blvd., Ste. 900, Houston, TX 77042, USA. (michael.glinsky@iongeo.com)

[5] In 3-D lock release of a turbidity current onto a plane, the system initially develops a cascade to small-scale turbulence. 3-D simulations [*Hartel et al.*, 2000; *Necker et al.*, 2002; *Cantero et al.*, 2007, 2008] show the system develops a set of large vortexes that effects the flow envelope and depends on R_e. Several stages take place in the flow depending on the front velocity [*Cantero et al.*, 2007, 2008]. Initially, the current accelerates; then the front velocity reaches a maxima; later the front velocity reaches a shallow minima; finally, the front velocity increases to a steady state. In the final steady state stage (slumping stage) large scale vortexes are formed and the small-scale turbulence has a small effect on the current shape and flow. After the steady state, there are two terminal stages. First, the current gradually slows down (inertial stage), then the flow slows down faster (viscous stage). During these terminal two stages there is a fast breakup of vortexes to small-scale turbulence which strongly affects the current shape and reduces the front velocity. In 2-D, there is no small-scale turbulence as in 3-D. The 2-D flow released from the lock accelerates and reaches a steady state front velocity stage as in the 3-D case for all R_e [*Hartel et al.*, 2000; *Necker et al.*, 2002]. In this stage the 2-D current behaves as the transverse average of the 3-D current. The steady state stage is the important stage for the formation of the sediment waves (SW) in the substrate. Therefore, in our study where we consider a 2-D lock release of large mass onto a plane that results in a steady state, self sustaining flow that generates the SWs, 2-D can replace 3-D for all R_e. During the terminal stages, when the front decelerates, the vortex coupling is stronger in 2-D than in 3-D, the flow energy cascade is different, and the front velocity in 2-D decays slower than in 3-D. At this stage, the flow shape in 2-D and 3-D become very different. We, therefore, conclude that 2-D simulations can replace 3-D simulations at the steady state stage when SWs are formed, for all R_e.

[6] In 3-D, the flow generates a shear layer close to the bottom boundary that is an ensemble of local turbulence of various types. This turbulence interacts with the substrate and causes a resuspension of particles. An empirical relation is applied to calculate the resuspension that depends on the shear velocity. In 3-D, the shear velocity can be calculated from the bottom flow velocity, including the effect of basal turbulence on the flow. In 2-D, the local turbulence and the generation of the shear layer do not exist so that a closure relation is required for the shear velocity that closes the set of flow equations. It is common to apply a phenomenological equation for the turbulent kinetic energy. The shear velocity is taken to be proportional to this energy. The turbulent kinetic energy includes source and sink terms due to the gain and loss from the resuspension and settling. This leads to the saturation of the net resuspension. The model was tested and found consistent with experiment [*Parker et al.*, 1986; *Pratson et al.*, 2001; *Kostic and Parker*, 2006]. A simplified version of the closure condition, that assumes a linear relation between the shear velocity and the bottom flow velocity, was validated against experiments [*Parker et al.*, 1986]. The constant of proportionality in this relationship is the bed drag coefficient. This is an approximate relation whose main disadvantages are that it is not coupled to a turbulence relation and that it does not include saturation of the resuspension. This simplified model, verified against experiment, is very useful in computation and therefore is applied in this work.

[7] The turbidity current code applied in this work is an extended version of the code developed and applied in *Blanchette et al.* [2005, 2006]. This code is based on the numerical model developed by *Hartel et al.* [2000] and *Necker et al.* [2002]. In *Blanchette et al.* [2005] validation of the numerical model was done by comparison with two experimental data sets and good agreement was obtained. A comparison was done for a lock release system of density currents measured experimentally by *Huppert and Simpson* [1980]. The front position as a function of time, for R_e = 6300, was compared. A further comparison was done for a particle driven current in a lock release mode. In this case, the deposit height as a function of position for several times (R_e = 2200) was compared to the experiment by *de Roojj and Dalziel* [2001]. A similar simulation was done also by *Necker et al.* [2002], but they considered the final deposition as a function of position for a 3-D simulation and found negligible differences with those computed in 2-D simulations.

[8] Numerical simulations have been carried out in order to explain the formation of SW by turbidity currents. The models can be divided into two categories: depth-averaged models, and depth-dependant models. The Navier-Stokes depth-averaged models perform 1D simulations of turbidity currents flowing downslope over an erodible bed. Pre-existing topography, such as surface roughness or a break in slope, are required to trigger the formation and growth of SW [*Kubo and Nakajima*, 2002; *Fildani et al.*, 2006; *Kostic and Parker*, 2006]. These models do not include the undulating structure in the turbulent flow imprinted by the SW periodicity. They also are unable to capture the detailed interaction between the sediment bed and the current close to the bed.

[9] A linear stability analysis (LSA) to generate SW based on the 2-D depth dependent Navier-Stokes equations was done by *Hall et al.* [2008], *Hall* [2009], and *Lesshafft et al.* [2011]. This is built on the classical work by *Flood* [1988]. Their results are consistent with a growth of the SW and their upstream migration. There are approximations made in this analysis. The front of the current is assumed to have passed so that the SW is growing underneath the body of the current. This analysis focuses on the structure of the basal boundary layer and its interaction with the substrate. This is in contrast to the analysis that will be carried out in this paper that focuses on the nonlinear interaction between the structure of the bulk flow and the substrate. They also use a simplified model of the linear erosion without a threshold. Finally, the expression used for the flow is an assumed perturbation that is linearly coupled to the substrate structure.

[10] We are motivated to eliminate the approximations used in these studies, and to obtain a more complete understanding of what controls the character of the SW generation. We therefore study SW using a geometry and computer simulation method that takes into account the non-linearity, uses a realistic erosion model, and models the depth dependant behavior in a nonlinearly self consistent and self generating way. In our treatment we apply nonlinear simulations based on the 2-D depth-dependent Navier-Stokes equations [*Hartel et al.*, 2000; *Necker et al.*, 2002; *Blanchette et al.*, 2005] with a realistic erosion relation [*Garcia and*

Parker, 1993; *Wright and Parker*, 2004; *Kostic and Parker*, 2006]. The model includes the effects of poly-disperse particles in the current and in the substrate, and a sequence of flows with a self consistent coupling to the substrate. An obstacle on the slope is used to trigger the possible buildup and possible growth of the SW. The flows are initiated from a lock release.

[11] We study the character of the SW generation as a function of four controlling parameters: (1) slope, (2) current lock height, (3) grain lock concentration, and (4) particle diameters. Three distinct phases of the SW generation are observed. Regions of the controlling parameter space are identified for each of the phases – the phase diagram. The boundaries between these regions are directly related to the self-sustainment of the flow. The first will be shown to be related to the flow being depositional everywhere on the slope, the second related to the flow being self sustaining only over the downslope part of the obstacle, and the third related to the flow being self sustaining everywhere. The first condition results in no SW formation, the second in the formation of a soliton like structure and the third with growing SW. The soliton like structure [*Ablowitz and Segur*, 1984], is a relatively constant periodic profile that migrates updip. This stable profile exists at the threshold between deposition and self-sustainment. The similarity to the buildup mode in a laser [*Arecchi et al.*, 1989], led us to calling it the SW buildup phase.

[12] The relationship of these solutions to the depth-averaged models is studied by forming depth-averaged variables from the detailed depth profiles. A periodic structure in the flow is noted. It is synchronized to the sediment waves in the substrate. No such structure is seen in the depth-averaged models. They have a very smooth character. This is not surprising since they do not incorporate the undulating structure. Similarly, including a diffusivity term in the transverse direction in the momentum equation as in *Felix* [2001] excludes the periodicity in the current velocity or concentration profiles.

[13] In the following sections we will present the physical model and numerical approach (section 2), followed by the simulations results (section 3) and concluding remarks (section 4).

2. Model Description

2.1. Governing Equations

[14] We consider a particle-laden turbidity current model for which the particle concentration is relatively low ($\sim$1%) and the density differences in the flow are sufficiently small. Hence, the density variation appears only in the gravity term (the Boussinesq approximation). We assume that the particles are small enough that the particle inertia can be ignored, allowing the particles to move in trajectories independent of the flow [*Druzhinin*, 1995]. The particles are transported by the current and settle relative to the fluid in the direction of the gravity vector. The system is assumed to be two-dimensional with normalized variables: $x = \tilde{x}/L_0$, $y = \tilde{y}/L_0$, and $t = \tilde{t}/t_0$, where $\tilde{x}$ and $\tilde{y}$ are the un-normalized space variables and $\tilde{t}$ is the un-normalized time variable. Here, a characteristic length scale, L_0, is used and the time is normalized as $t_0 = L_0/u_b$. For the purpose of our study a value of L_0 = 250 m will be considered, giving a characteristic SW wavelength of 350 m. The buoyancy velocity is defined as

$$u_b = \sqrt{R_* c_0 g L_0}, \tag{1}$$

where g is the gravity constant, c_0 is the initial grain concentration in the lock, $R_* = (\rho_p - \rho_f)/\rho_f$ is the fractional density difference, ρ_p is the grain particle density, and ρ_f is the fluid density. The concentration of grain type i, $\tilde{c}_i$, is normalized to give $c_i = \tilde{c}_i/c_0$. The variable x is in the local flow direction, y is in the perpendicular direction and θ is the local angle between the direction of gravity and the negative y direction. In order to model complex topographies we use a spatially varying gravity vector with and angle θ [*Blanchette et al.*, 2005, 2006]. A curvilinear coordinate system is simulated with the second order curvatures being neglected. This approximation is valid for flow heights smaller than the radius of curvature of the bottom topography.

[15] The current equation, in normalized units, are written in terms of the vorticity, ω, and the stream function, ψ,

$$u_x = \frac{\partial \psi}{\partial y}, \tag{2}$$

$$u_y = -\frac{\partial \psi}{\partial x}, \tag{3}$$

$$\omega = \frac{\partial u_y}{\partial x} - \frac{\partial u_x}{\partial y}, \tag{4}$$

where $u_x = \tilde{u}_x/u_b$ and $u_y = \tilde{u}_y/u_b$ are the normalized velocities. These equations are consistent with the continuity equation

$$\frac{\partial u_x}{\partial x} + \frac{\partial u_y}{\partial y} = 0. \tag{5}$$

[16] The resulting current equations for ω, ψ, and c_i are [*Hartel et al.*, 2000; *Necker et al.*, 2002; *Blanchette et al.*, 2005]

$$\frac{\partial \omega}{\partial t} + (\vec{u} \cdot \nabla)\omega = \frac{1}{R_e}\nabla^2 \omega + (\hat{g} \times \nabla c)_z, \tag{6}$$

$$\nabla^2 \psi = -\omega, \tag{7}$$

$$\frac{\partial c_i}{\partial t} + (\vec{u} + u_{si}\hat{g}) \cdot \nabla c_i = \frac{1}{P_e}\nabla^2 c_i, \tag{8}$$

where $c = \sum_i c_i$ is the normalized concentration of grains in the current (initially c = 1), and $\hat{g} \equiv (\sin\theta, -\cos\theta)$ is a unit vector in the direction of gravity. Equation (6) is obtained from the Navier-Stokes momentum equation and includes the 2-D vorticity of the flow. Equation (7) is obtained from equations (2)–(4). In these equations we have used the system's Reynolds number, $R_e = u_b L_0/\nu$, where ν is the fluid viscosity. The Peclet number $P_e = S_c R_e$ is related to the Schmidt number, $S_c = \nu/\kappa$, where κ is the particle diffusion constant. We assume that small scale unresolved flow structure will affect the transport of particles in the same way as the transport of the fluid, so we set $P_e = R_e$ or $S_c = 1$ [*Hartel et al.*, 2000]. The settling velocity, $\tilde{u}_{si}$, for grain type i is normalized to be $u_{si} = \tilde{u}_{si}/u_b$. Note that the driving force of the current, in equation (6), comes from the variation in the concentration c perpendicular to $\hat{g}$.

[17] We use the convention that the dependant and independent variables of the PDEs (partial differential equations) have tildes, if they have dimensions, and are dimensionless without. Constants of the PDEs (such as R_e) and constants used to scale the variables (such as g, ν, κ, L_0, t_0, u_b, and c_0) are always used without tildes to keep the notational complexity to a minimum.

[18] The exchange of particles between the substrate and the current is governed by an Exner type equation for the substrate elevation $\eta(x, t)$ in accordance with the sediment transport rate [*Parker et al.*, 2000; *Pratson et al.*, 2001]

$$\left(1-\lambda_p\right)\frac{\partial\eta}{\partial t} = \sum_i \left(J_{si} - J_{ri}\right), \tag{9}$$

where J_{si} and J_{ri} are the volume rate of deposition and resuspension from the substrate surface for grain type i, respectively. The sum in equation (9) is over all types of grains, i, and λ_p is the average substrate porosity. Here η is normalized by a length $s_0 = L_0c_0/(1 - \lambda_p)$, where λ_p is the porosity. For typical values of $L_0 = 250$ m, $c_0 = 0.8\%$, and $\lambda_p = 0.3$, we obtain $s_0 = 2.9$ m. The substrate is divided into an upper and lower layer, where the upper layer is an active layer (AL) with thickness L_a. Exchange of particles between the substrate and the current takes place via this layer.

[19] We use, for the current, a rectangular computational domain. At the boundary, we enforce a non-slip, no normal flow condition, $\psi = \partial\psi/\partial y = 0$, at the top and bottom boundaries. We also impose a no normal flow condition at the left and right walls so that $\psi = \partial^2\psi/\partial x^2 = 0$. This allows the use of fast Fourier transforms in the x direction for high accuracy [*Hartel et al.*, 2000; *Blanchette et al.*, 2006].

2.2. Physical Mechanisms

2.2.1. Resuspension Term

[20] The exchange of particles between the current and the substrate includes settling and resuspension contributions. For grain type i the normalized exchange current, J_i, is

$$J_i = J_{si} - J_{ri} = u_{si}\left(-\hat{g}_y c_b - \varepsilon_{si}\right), \tag{10}$$

where J_{si} is the settling flux of grain type i with a settling velocity, u_{si}, such that

$$J_{si} = -u_{si}\hat{g}_y c_b, \tag{11}$$

with c_b being normalized grain volume concentration close to the bottom of the current and $\hat{g}_y = -\cos\theta$. The resuspension current of grains of type i is

$$J_{ri} = u_{si}\varepsilon_{si}, \tag{12}$$

where ε_{si} is the normalized resuspension volume. From their laboratory experiments, *Garcia and Parker* [1993] derived the resuspension relation

$$\varepsilon_{si} = \frac{a}{c_0}\frac{z_i^5}{1+\frac{a}{0.3}z_i^5}f_{ri}, \tag{13}$$

where f_{ri} is a resuspension factor equal to the relative presence of grain type i in the active layer at the substrate surface. The factor a in equation (13) for field scale can be increased by a factor of 6 [*Wright and Parker*, 2004], but can also be reduced by a similar factor due to sediment strength – the entrainment limiter [*Kostic and Parker*, 2006; *Fildani et al.*, 2006]. For simplicity, we use the older value $a = 1.3 \times 10^{-7}$ [*Garcia and Parker*, 1993] in our calculation. The expression for z_i is

$$z_i = \alpha_1\frac{u*}{u_{si}}R_{pi}^{\alpha_2}, \tag{14}$$

where R_{pi} is the particle Reynolds number,

$$R_{pi} = \sqrt{R*gd_i}\frac{d_i}{\nu}, \tag{15}$$

d_i is the diameter of grain type i, and $u* = \tilde{u}*/u_b$ is the normalized shear velocity at the boundary which can be written in normalized variables as [*Blanchette et al.*, 2005]

$$u_* = \sqrt{\frac{1}{R_e}\frac{\partial u_x}{\partial y}}. \tag{16}$$

[21] We use values for α_1 and α_2 from experiments by *Garcia and Parker* [1993]

$$(\alpha_1, \alpha_2) = \begin{cases} (1, 0.6) & R_p > 2.36 \\ (0.586, 1.23) & R_p \le 2.36 \end{cases}. \tag{17}$$

In equation (14), for the geophysical field currents, a slope dependence term $\theta^{0.08}$ of order unity is ignored [*Kostic and Parker*, 2006]. Equation (13) has a high power in z_i and therefore behaves as a threshold relation for the resuspension as a function of $(u*/u_{si})^5$.

2.2.2. Active Layer

[22] We apply an active layer (AL) in the substrate surface from which resuspension can take place. Its dimension depends on the resuspension strength [*Parker et al.*, 2000]. The AL can have a very large range in depth, from the size of a few grains, in the case of turbidity currents, to the size of the width of the flow, in the case of fluvial flows. We assume that the flow can mix the particles in the AL, generating a uniform distribution of all grain types in this layer.

[23] The mixing mechanism in the AL can be due to grain traction or small scale topographic variations of the substrate surface. For example, small scale dunes can accumulate coarse grains in the local minima and fine grains in local maxima. The AL width would be the long range average distance of these local maxima and minima [*Parker et al.*, 2000]. All the grains in the AL are available for resuspension by interaction with the current turbulence. Resuspension causes a decrease in the upper boundary height of the substrate and for a given AL width, deeper parts of the substrate can now be included in the AL. Deposition increases the substrate height so that deeper parts of the substrate must now be excluded from the AL. We include in the computation an AL model capable of handling very small, $L_a \ll 1$, and very large, $L_a \gg 1$, active layers.

[24] In our simulations, we divide the substrate into zones of size Δs perpendicular to the substrate surface, where the

upper zone may be partially filled. Typically zones are $\Delta s \approx 0.1$ in normalized units. The AL can be very large and include many zones, or can be very small and encompass just a fraction of a single zone. The upper boundary of the substrate is the upper boundary of the AL. The lower boundary of the AL is obtained by subtracting the AL width, L_a, from the upper boundary. The lower boundary can be in the same zone as the upper boundary or in a much lower zone. Every time step, we sum over the resuspension and deposition mass, obtain the new upper level of the substrate, and define the AL range. A mixing process is then applied to the AL to make the grain type distribution uniform from the bottom to the top of the AL.

[25] Armoring happens when fine grains can be resuspended, while coarse are being deposited by the flow. This will leave an AL made up of only coarse grains which will not be able to be resuspended. This turns off the resuspension, changing the flow into a purely depositional one. The result is a dissipating current and reduction in the front velocity.

2.2.3. Settling Velocity

[26] The settling velocity, $\tilde{u}_{si}$, for grain type i is obtained by using the relationship from *Dietrich* [1982]

$$\tilde{u}_{si} = \sqrt[3]{R_* g \nu W_i}, \tag{18}$$

where

$$\log_{10} W_i = -3.76715 + 1.92944\ A - 0.09815\ A^2 - 0.00575\ A^3 + 0.00056\ A^4, \tag{19}$$

$A = 2\log_{10} R_{pi}$, and the particle Reynolds number, R_{pi} is defined by equation (15). The normalized settling velocities, $u_{si} = \tilde{u}_{si}/u_b$, depends on the input parameters of the particles. Here, R_{pi} can be identified as the normalized version of the particle diameter, d_i.

2.2.4. Shear Factor

[27] In 3-D simulations, high R_e turbulence motion generates a shear layer at the bottom of the flow. This layer affects the shear velocity close to the boundary. In 2-D, there is no local turbulence and the shear velocity needs to be evaluated in away that is consistent with experiments. To define an appropriate shear velocity, a shear factor is introduced. It is similar to the parameter in other models called the bed resistance coefficient or the bottom drag coefficient, C_D [*Parker et al.*, 1986]. The shear factor, f_{shr}, is used to obtain the appropriate shear velocity, u_*, to avoid unrealistic resuspension in the simulations. We include in equation (16) a shear factor, f_{shr}, such that

$$u_*^2 = \frac{\omega_b}{f_{\text{shr}} R_e}, \tag{20}$$

where ω_b is the vorticity close to the bottom, R_e is the Reynolds number, and equation (4) has been used. The shear friction force at the bottom of the flow is proportional to u_*^2. Other models such the $\kappa - \varepsilon$ turbulence model [*Felix*, 2001; *Choi and Garcia*, 2002; *Huang et al.*, 2000] and the depth-averaged model [*Parker et al.*, 1986] do not have a shear factor. Instead, they have C_D. We will show that there is a simple relationship between our shear factor, f_{shr}, and C_D. Therefore, our treatment of the turbulence with a shear factor is directly related to these alternative treatments.

[28] The equivalent parameter in the other models is defined as

$$C_D \equiv \left(\frac{u_*}{v_b}\right)^2, \tag{21}$$

where v_b is the flow velocity at the grid closest to the bottom current. The relation between v_b and ω_b is

$$\omega_b = \left(\frac{\partial u_x}{\partial y}\right)_b = \frac{v_b}{\Delta_y}, \tag{22}$$

where Δ_y is the zone height, and $u_x = 0$ at the bottom.

[29] In the $\kappa - \varepsilon$ turbulence model *Felix* [2001] and *Choi and Garcia* [2002] use equation (21) to obtain the u_* used in the resuspension relation and approximate C_D by

$$C_D = \left(\frac{1}{\kappa}\ln(Ez_b/z_0)\right)^{-2}, \tag{23}$$

where $\kappa = 0.4$ is the von Karman constant, E is the roughness parameter (which varies between 9 to 30 going from smooth to rough walls), z_b is the height of the lowest grid cell, z_0 is the roughness height (for a smooth bottom $z_0 = \nu/u_*$), and ν is the fluid viscosity. For our case with a scale length of 250 m, 64 zones per unit (that is $z_b = 3.9$ m), $E = 10$, and $z_0 = 10^{-3}$ m, we get $C_D = 1.4 \times 10^{-3}$. *Felix* [2001] using equation (23) obtains $C_D = 2.5 \times 10^{-3}$. *Garcia and Parker* [1993] predict that for currents with Reynolds numbers $R_e \approx 10^3$ to 10^5, $C_D \approx 0.1$ to 10^{-3}.

[30] *Parker et al.* [1986] depth averaged model used three transverse average equations (for height, h, velocity, U, and concentration, C) and used equation (21) as a closure condition with $C_D = 4 \times 10^{-3}$. They also extended the model to four equations, adding an equation for the turbulence energy, k. Assuming that $C_D = \alpha k$ with $\alpha = 0.1$, they found that C_D varied in the range of approximately 0.1 to 10^{-3}.

[31] For our case, we evaluate C_D using equations (20)–(22) and obtain

$$C_D = \frac{1}{f_{\text{shr}} R_e \Delta_y v_b}. \tag{24}$$

Substituting our simulation parameters ($R_e = 10^3$, $f_{\text{shr}} = 38$, $\Delta_y = 1/64$, and $v_b = 0.1$) into this equation we get $C_D = 1.7 \times 10^{-2}$.

[32] For our simulations, we evaluated equation (21) over a wide range of locations, x, and times, t. We found that C_D varies between about 0.1 to 10^{-3}. We therefore conclude that f_{shr} used in our model produces resuspension though a u_* similar to the resuspension obtained in the previous models using C_D.

2.3. Numerical Approach

[33] The numerical methods used to solve the current equations (6)–(8) are based on *Lele* [1992], *Hartel et al.* [2000], and *Blanchette et al.* [2005]. We perform a Fourier transform on ψ in the x direction and use a sixth-order finite difference scheme for the derivatives in the y-direction, except near the boundaries where the derivatives are accurate to third order. A third-order Runge-Kutta integrator is used to propagate the solution in time. A finite difference

time integrator is applied to equation (9) to update the substrate particle budget, and an AL scheme is applied in the determination of the balance between erosion and deposition. The finite difference time integrator is implemented by replacing $\partial\eta/\partial t$ by $\frac{\eta(t+\Delta t)-\eta(t)}{\Delta t}$. An adaptive time step is used which satisfies the Courant-Friedrichs-Levy condition to minimize the computation time. A typical time step is at $\Delta t \approx 0.01$. For a typical length scale $L_0 = 250$ m and buoyancy velocity $u_b = 5$ m/s, we get a timescale of $t_0 = L_0/u_b = 50$ s. The length scale, $L_0 = 250$ m, is selected to obtain simulated SW consistent with the field observation of SW wavelength, $\lambda = 350$ m.

[34] Typically, the fluid equations are solved over a rectangular domain ($-4 \leq x \leq 23$ and $0 \leq y \leq 3$) divided into 513 and 193 grid cells, respectively. When the number of grid cells in the x and the y directions were doubled there was no change in the results. We therefore conclude that the results have converged and this resolution is sufficient. An additional rectangular grid is used for the substrate at the same x locations and over a range, in the perpendicular direction, of $0 < s < 20$, where the distance is scaled by $s_0 = L_0 c_0/(1 - \lambda_p)$ with a porosity of $\lambda_p = 0.3$. The substrate is divided into 513 and 601 grid cells in the x and s directions, respectively. An AL is applied of height $L_a = 0.02$. Changing L_a by a factor of 2 has a small effect on the results.

[35] A lock release is simulated where the fluid is initially located at rest in a typical range of $-4 \leq x \leq 0$ and $0 \leq y \leq 1.5$, with a fluid height of $y = 3$. We consider a lock of 4 units wide and 1.5 units in height. For a scale length of $L_0 = 250$ m this is a reservoir 1 km long and 375 m high, which gives an episodic geophysical turbidity current extending for many kilometers. To obtain a sustained current of much longer time a different boundary condition for the flow needs to be considered – a steady state inflow to the system. This boundary condition is not included in the present study.

[36] It was shown by *Blanchette et al.* [2005] that the effect of the upper fluid boundary can be neglected if it is at least twice the height of the lock release, that is it can be considered a deepwater case. For numerical stability the initial lock particle concentration profile and the substrate bottom topography is smoothed over a few grid points (typically 6). The typical initial volume concentration is $c_0 = 0.8\%$.

[37] The value of Reynolds numbers, $R_e = u_b L_0/\nu$, for geological turbidity currents with u_b in the range of 1 m/s to 5 m/s, scale lengths, L_0, in the range of 1 m to 250 m, and a water viscosity of $\nu = 10^{-6}$ m^2/s, are in the range 10^6 to 10^{10}. These Reynolds numbers are well beyond the reach of numerical simulation. As R_e increases, smaller scales must be resolved, which also implies smaller time steps as well as more grid cells. All the simulations are done in 2-D for a relatively low Reynolds number $R_e = 1000$. In this case, the vortex structure of the flow is not as fully developed as for high R_e. It is found, that in 2-D, the front velocity and the front shape is almost independent of R_e [*Hartel et al.*, 2000; *Necker et al.*, 2002; *Blanchette et al.*, 2005]. There is a self-consistent coupling between the flow and the substrate. For many sequential flows, the affect of the substrate from the accumulated SW can have a large imprint on the current profile. This can cause the flow profile to adapt itself to the undulating substrate, even for high R_e. We expect that the simulation of many consecutive flows, with $R_e = 1000$, will qualitatively include this feature of high R_e. To make the flow more realistic, we include a shear velocity that is consistent with field observations by introducing a shear factor, equation (20) consistent with the bed drag coefficient applied by others, equation (21). Three movies, one for each phase corresponding to the three substrate profiles shown in Figure 5, can be found in the auxiliary material.[1]

[38] To obtain physical resuspension, we use a shear factor of $f_{\rm shr} = 38$. The eroded particles are spread uniformly in a region close to the substrate, typically over a thickness of 0.15. Changing the spreading range by 20% only has a small effect on the results. When the resuspension is high, the particles injected over this range are rapidly transported further by the flow to distances much greater than the initial injection range. This leads to the small sensitivity to the initial injection range. In contrast, depth-averaged models the injected particles are spread over the transverse layer.

[39] Five types of grains are simulated with diameters that range from 300 μm to 1000 μm. The number of flows simulated are typically 120. A typical runtime on an 8 core (dual quad core Xeon E5462, 2.68 GHz) machine is 20 hours. The program is restartable.

2.4. Transverse Average Current Variables

[40] To study the current structure and compare it to previous work, we depth average the transverse current profiles in the y-direction as a function of x. In the appendix of the paper by *Parker et al.* [1986], they write the depth-averaged variables for the velocity, U, height, h, and concentration, C, in terms of the local velocity, u_x as

$$U\ h = \int_0^{y_l} u_x dy = a_1, \tag{25}$$

$$U^2\ h = \int_0^{y_l} u_x^2 dy = a_2, \tag{26}$$

and

$$U\ C\ h = \int_0^{y_l} u_x c\, dy = a_3, \tag{27}$$

where y is the transverse coordinate, u_x is the velocity in the longitudinal x-direction, and c is the normalized concentration. Here, y_l defines the range in the y-direction of appreciable concentration in the current, $c > c_l$ [*Middleton*, 1993]. We use a value of $c_l = 3/4$, relative to the initial concentration of 1. The transverse layer average values for U, h, C obtained from equations (25)–(27) are

$$U = \frac{a_2}{a_1}, \tag{28}$$

$$h = \frac{a_1^2}{a_2}, \tag{29}$$

and

$$C = \frac{a_3}{a_1}. \tag{30}$$

[1]Auxiliary materials are available in the HTML. doi:10.1029/2011JC007539.

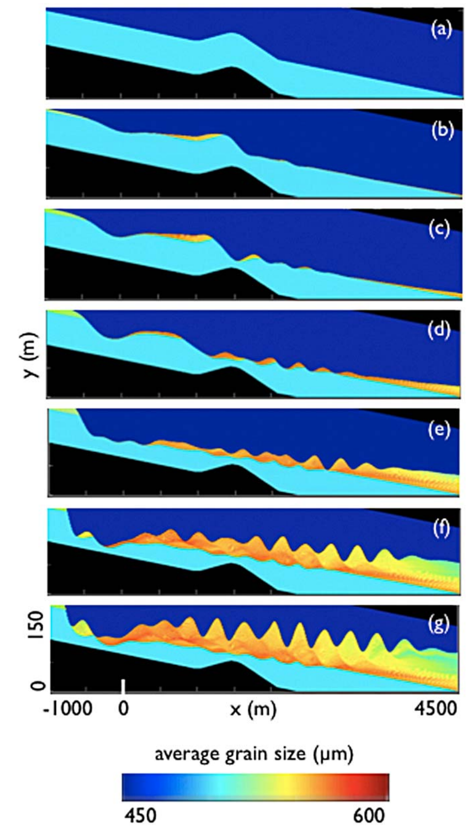

Figure 1. Development of sediment waves on the substrate. The *x-y* image is colored according to the average grain diameter. The color bar is a rainbow, starting from 450 μm at blue and ending at 600 μm at red. The profiles are shown after: (a) 1, (b) 5, (c) 10, (d) 20, (e) 40, (f) 80, and (g) 120 flows. The initial slope is θ_0 = 1.5°, and the flows include 5 types of grains with diameters that range from 300 μm to 700 μm (R_{pi} = 20 to 71). Initially there is an obstacle between x values of 1000 m and 2000 m with a peak at 1500 m (in normalized units: 4, 8, and 6). The upstream slope of the obstacle is −2°, and the downstream slope is 5°. The lock is between −1000 m and 0 m ($-4 < x < 0$) with an initial height of 375 m (H = 1.5) and particle concentration of c_0 = 0.8%.

[41] Averaging the simulation profiles of u_x with equations (25)–(27), the transverse average variables U, h, and C are obtained by using equations (28)–(30).

[42] The depth-average variables are used to calculate the local Richardson number

$$Ri = \frac{1}{F_r^2} = \frac{R_* gCh}{U^2}, \qquad (31)$$

where F_r is the local Froude number. We define F_2 as

$$F_2 \equiv \frac{1}{Ri} - 1. \qquad (32)$$

The square of the Froude number is proportional to U^2/h and indicates the ratio of the kinetic energy of the flow to the potential energy of the fluid. For $Ri < 1$, $F_r > 1$, or $F_2 > 0$ the local current is supercritical, that is the kinetic energy of the flow is greater than the potential energy of the fluid. It is usually assumed [*Parker et al.*, 1986] that a supercritical flow is predominately erosional and that a subcritical flow, $F_2 < 0$, is predominately depositional.

[43] Even though the depth-averaged variables only show the characteristics of the envelope of the current, we will find that the undulating structure has an imprint on the average velocity, U, and average height, h. There are periodic structures on these variables correlated with both the sediment waves and undulating structure of the current. A convergence of the flow toward the substrate reduces h and increases U causing a peak in F_2. This peak correlates with a peak in the shear velocity, u_*, and with a resulting increase in resuspension. In the next section we will present the depth average variables $U(x)$, $C(x)$, and $h(x)$, obtained from the detailed current profile, as functions of the location x. We will also present the local Froude number dependance as $F_2(x)$ (remember that $F_2 > 0$ indicates supercritical flow locally and $F_2 < 0$ indicates locally subcritical flow), and the local $u_*^5(x)$ (indicating the local shear velocity dependance of the resuspension, see equations (13) and (14)).

3. Simulation Results for Sediment Wave Generation

3.1. Effect of an Obstacle

[44] We simulated multiple lock release flows down a 2-D "channel" in the *x-y* plane of dimension $-4 < x < 23$ and slope θ_0 = 1.5°, where the scale length for x and y is L_0 = 250 m. The flow and the substrate initially include 5 types of grains equally distributed with diameters of $\{d_i\}$ = {300, 400, 500, 600, 700} μm. This corresponds to particle Reynolds numbers, R_{pi}, that range from 20 to 71. The suspension in the lock is located in the area where $-4 < x < 0$, $0 < y < H$, and H = 1.5. The water boundary is at y = 3, which is large enough to cause little coupling of the flow to the water boundary—a deepwater flow. The initial particle concentration in the lock is c_0 = 0.8%. An obstacle of triangular shape with rounded corners is located along the channel at $\{x_i\}$ = {4, 6, 8} = {start, top, end} with an angle of −2° on the upstream side and 5° on the downstream side. The current is absorbed exponentially as a function of time at the end of the channel in the range of x = 19 to 23. First the resuspension is turned off exponentially in the range of x = 19 to 20, later the concentration is reduced exponentially in the range of x = 20 to 23. The exponential decay factor used is 5. The initial substrate and obstacle structure is presented (in real units) in Figure 1a.

[45] Figure 1 presents the substrate structure and the development of the sediment wave along the channel in the *x-y* plane for up to 120 sequential flows. Each flow has been completed before the next is started. The substrate is colored according to the average grain diameter over the range of 450 μm to 600 μm. Considering the particle diameter distribution in the substrate, by examining its width or variance, we find similar behavior. For the fifth flow, f = 5, there is deposition before the obstacle crest and erosion after the crest. The extra erosion downstream generates the next break (increase) in slope and starts the next crest in the downstream direction. For f = 10 and f = 20 a train of breaks (increase) in slope develop seeding the SW structure. Every SW crest moves upstream due the current deposition on the

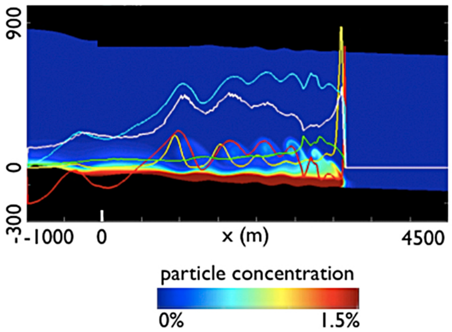

Figure 2. Particle volume concentration of the flow in the x-y plane at the normalized time, $t = 8$, for flow, $f = 20$ (timescale is $t_0 = L_0/u_b = 46$ s, buoyancy velocity is $u_b = \sqrt{gR_* c_0 L_0} = 5.42$ m/s, particle density change relative to water is $R_* = 1.5$, and initial particle concentration is $c_0 = 0.8\%$). This corresponds to Figure 1d. The color bar is a rainbow, starting from 0 at blue and ending at 1.5% at red. Also shown are the depth averaged current variables: (blue) velocity $U \times 100$ in m/s, (white) concentration $C \times 2 \times 10^4$, (green) current height h in m, (red) change in Froude number $F_2 \times 200$, and (yellow) shear velocity term in the resuspension $V_{\text{shr}}^5 \times 5 \times 10^6$ in (m/s)^5. All quantities plotted have SI dimensions.

upstream side of the crest and the erosion on the downstream side. By $f = 40$ a well developed SW train is formed, propagating downstream by the seeding of new breaks in slope, and migrating upstream by the structured erosion and deposition. By $f = 80$ and $f = 120$ the upstream SW are effected by erosion close to the lock boundary. The downstream part of the SW starts to be affected by the change in slope due to current reflection and deposition at the right boundary. Increasing the channel length extends the range of the SW downstream, but does not effect the general structure of the flows that we will analyze. In the figures presenting the development of SW in the substrate, as in Figure 1, we consider the color map of the average grain size diameter.

[46] Figure 2 presents contours of the current's particle concentration in the x-y plane at the normalized time, $t = 8$, for flow, $f = 20$. The current head has already passed over the obstacle. The timescale is $t_0 = L_0/u_b = 46$ s, the length scale is $L_0 = 250$ m, the buoyancy velocity is $u_b = \sqrt{gR_* c_0 L_0} = 5.42$ m/s, $g = 9.81$ m/s^2, and the particle density change is $R_* = 1.5$. The image colors are the particle volume concentration in the range of 0 to 1.5%. Also shown in Figure 2 are the transverse average variables as a function of x: the current velocity $U(x)$ in blue, the concentration $C(x)$ in white, the current height $h(x)$ in green, the change in the Froude number $F_2(x) = F_r^2 - 1 = 1/Ri - 1$ in red, and the shear velocity term in the resuspension expression V_{shr}^5 in yellow. Note that SW periodicity in the substrate is coupled into the current and appears as an undulating structure in the current and as a periodicity in the transversely averaged variables. The generated undulating structures are mainly seen at the top part of the flow. Characteristic values for the flow are $U \approx 4.5$ m/s, $C \approx 1.5\%$ (twice its initial value), and $h \approx 60$ m. The Froude number is greater than 1 for a large part of the flow (supercritical) and the flow is highly erosive. Note that the amount erosion is not well correlated with the degree of supercriticality. There is also an exponential growth in the erosion as one goes from the head to the tail of the flow, while the change is the Froude number is relatively constant. The wavelength of the SW is consistent with the *Normark et al.* [1980] relation, $\lambda = 2\pi h$, where $\lambda = 380$ m for $h = 60$ m.

[47] One limitation of the computational model is that the radius of curvature R_t of the bottom topography should be larger than the current height, h. Here $R_t = \pi x_t/2\theta_t$ and $\theta_t = 2h_t/x_t$ is the curvature angle, where x_t is the curvature length and h_t is the topography height. For a SW substrate $x_t \approx \lambda/2$, where λ is the wavelength of the SW and h_t is the SW topography height (difference between maxima and minima height). Typically, in normalized units with $L_0 = 250$ m, $\lambda \approx 1.5$. After 80 flows, we get $h_t \approx 0.12$ and $R_t = 3.7$, which is larger than a typical current height, $h = 0.4$, and even larger than the flow domain height, $H_0 = 3$.

[48] Figure 3 shows the total mass in the flow, $m(t)$, and its front position, $x_{\text{tip}}(t)$, as a function of time for flows $\{f\} = \{1, 20, 40, 80, 120\}$. For flows 1 and 20, there is an increase in the total mass, because of resuspension, by almost a factor of 2. The current asymptotes to a speed of about 4.5 m/s. The resuspension maintains the current motion and redistributes the substrate mass to form the growing SW. For later flows (40, 80, and 120), the substrate slope is reduced by deposition at the end of the channel. Consequently, the resuspension and the growth of the SW are reduced, keeping the

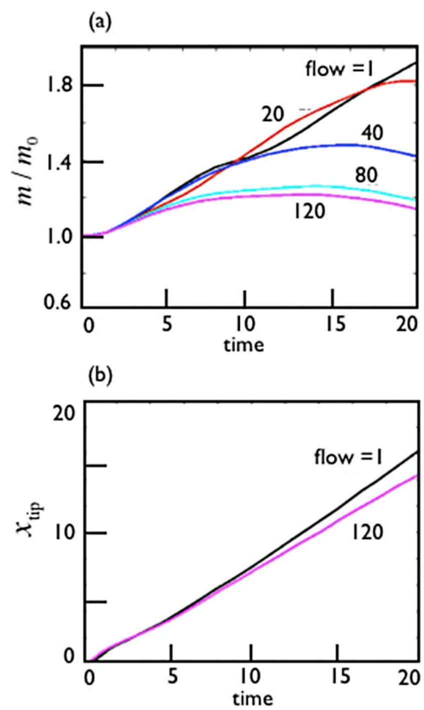

Figure 3. (a) Normalized suspended mass in flow as a function of time, $m(t)/m_0$, for flows: (black) 1, (red) 20, (blue) 40, (cyan) 80, and (magenta) 120. Time is plotted in normalized units (the scale for time is $t_0 = 46$ s). (b) Front position as a function of time, $x_{\text{tip}}(t)$, for flows: (black) 1 and (magenta) 120. The front velocity is reduced from 0.90 for flow 1, to 0.73 for flow 120. In dimensional units, these are velocities of 4.9 m/s and 3.9 m/s ($u_b = 5.42$ m/s).

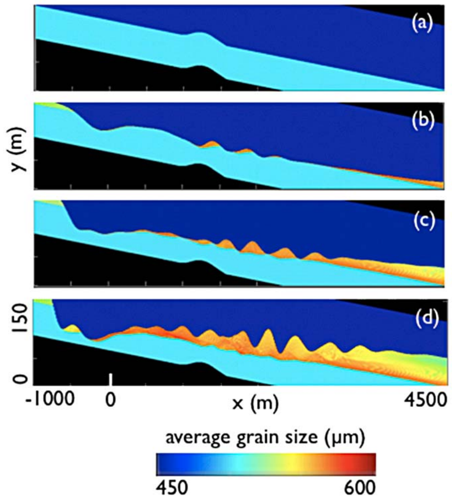

Figure 4. Development of sediment waves on the substrate with a reduced size obstacle (by a factor of 2). Initially there is an obstacle between x values of 1000 m and 1500 m with a peak at 1250 m (in normalized units: 4, 6, and 5). The upstream slope of the obstacle is $-2°$, and the downstream slope is $5°$. The x-y image is colored according to the average grain diameter. The color bar is a rainbow, starting from 450 μm at blue and ending at 600 μm at red. The profiles are shown after: (a) 1, (b) 10, (c) 40, and (d) 80 flows. Other than the size of the obstacle, all parameter are identical to the simulations shown in Figures 1 to 3.

mass in the flow constant and changing only the sediment wave structure.

[49] Figure 4 shows the result of reducing the obstacle height and width by a factor of 2, located at $\{x_i\} = \{4, 5, 6\}$ with angles $\{\theta_i\} = \{-2°, 5°\}$. All other parameters are the same as the previous simulation. Reducing the obstacle size has only a small effect on the growing SW. Comparing Figure 4 to Figure 1 for flow 80, we find a very similar SW development. The obstacle's function is to trigger the probable growing wavelength. By flow 10, the obstacle is eroded leaving the system to develop SW independent of the initial condition.

3.2. Influence of Lock Height

[50] We now present a series of systematic parameter studies over the next three subsections of the paper. We start with examining the influence of lock height, H, on the character of the flow and SW formation. The lock height is directly related to the size of the flow. Three characteristic lock heights (0.5, 1.0, and 1.5) are simulated for the reduced obstacle system displayed in Figure 4. The results are shown in Figures 5–7. The slope angle was also changed for each of the cases to 0.5°, 0.5° and 1.5°, respectively. This was done to access the three different phases of SW development.

[51] Previous studies [*Blanchette et al.*, 2005] found little dependence on the aspect ratio of the flow, W/H. When we doubled the width of the flow from 4 to 8 units, keeping the total mass, WH, constant, we found little change in the sediment wave structure. Specifically, there was not a significant change in the wavelength. Therefore, systematically changing the lock height, H, is a surrogate for changing the total mass, WH.

[52] For the first case (Figure 5a), there was no sediment wave formation. We call this the "no SW" phase. It is characterized by a final uniform slope topography. As more flows are deposited the obstacle is removed from the topography. Further characteristics of this phase can be seen in Figures 6a and 7. Figure 6 shows the profile of the particle concentration in flow and the depth averaged current variables in the same manner as Figure 2. The time evolution of the suspended mass in the flow, $m(t)$, and the front position, $x_{\mathrm{tip}}(t)$, are shown in Figure 7 in the same manner as Figure 3. Note the simple structure to the flow in Figure 6a. The flow is divided into the head with an elevated velocity and concentration. It is modestly supercritical as evidenced by F_2. The head is followed by a subcritical body. There is no appreciable erosion as evidenced by the small values of V_{shr}^5. There is little structure within these two parts of the flow. Figure 7 shows a monotonically decreasing mass and a reduced front velocity of 0.42 in normalized units and 2.3 m/s in dimensional units. An important thing to note about this phase is that the initial substrate is at no point steep enough in slope to support self sustainment according to the criterion presented in *Blanchette et al.* [2005]. This criterion gives the critical angle, θ_c, for self sustainment as a function of c_0, H, and d. The characteristics of the deposited beds shown in Figure 5a, are quite simple. Even though there have been many flows there appears to be one massive bed that becomes gradually more fine grained downslope and gradually more coarse grained going from the bottom to the top of this massive bed.

[53] The second phase is demonstrated in Figures 5b, 6b, and 7. We call this phase "SW buildup". This phase is characterized by the obstacle being reorganized by the early flows into a stable self-consistent profile that neither grows

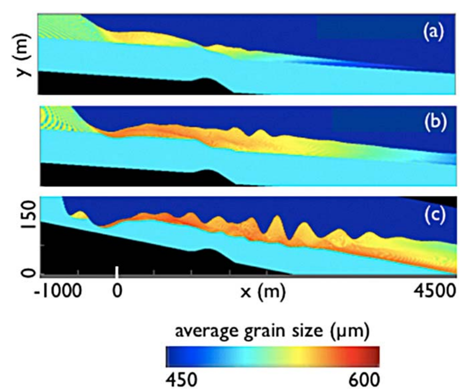

Figure 5. Development of SW on a substrate after 80 flows, to study the effect of the initial height, H. The x-y image is colored according to the average grain diameter. The initial obstacle has the reduced height shown in Figure 4. The color bar is a rainbow, starting from 450 μm at blue and ending at 600 μm at red. The profiles are shown for: (a) "no SW," H = 0.5, θ_0 = 0.5°; (b) "SW buildup," H = 1.0, θ_0 = 0.5°; and (c) "SW growth," H = 1.5, θ_0 = 1.5°. Auxiliary material consists of three movies of the substrate evolution leading to these three substrate profiles. Auxiliary material consists of three movies of the substrate evolution leading to these three substrate profiles.

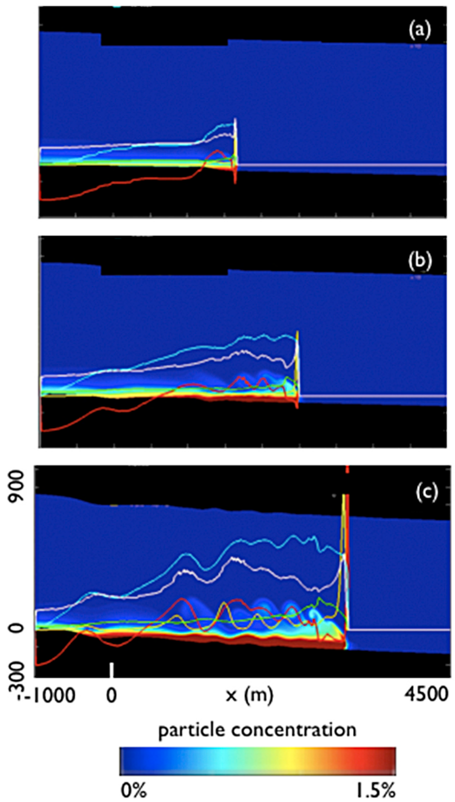

Figure 6. Particle volume concentration of the flow in the x-y plane at the normalized time, $t = 8$, for flow, $f = 15$, to study the effect of the initial height, H. This corresponds to simulations of Figure 5. The color bar is a rainbow, starting from 0 at blue and ending at 1.5% at red. Also shown are the depth averaged current variables: (blue) velocity $U \times 100$ in m/s, (white) concentration $C \times 2 \times 10^4$, (green) current height h in m, (red) change in Froude number $F_2 \times 200$, and (yellow) shear velocity term in the resuspension $V_{\rm shr}^5 \times 5 \times 10^6$ in (m/s)^5. All quantities plotted have SI dimensions. The profiles are shown for: (a) "no SW," $H = 0.5$, $\theta = 0.5°$; (b) "SW buildup," $H = 1.0$, $\theta = 0.5°$; and (c) "SW growth," $H = 1.5$, $\theta = 1.5°$.

or decays with additional flows. It should be noted that the initial substrate profile is only steep enough on the downstream side of the obstacle to support self sustainment. We recognize that this profile is maintained on the boundary of SW growth where the resuspension leading to growth is balanced by the deposition favoring decay. Because of this and the invariant profile that we call this phase soliton like. In addition, it is very similar to the buildup mode in a laser. In a buildup mode, random perturbations in the laser cavity are self organized into a persistent organized mode in the laser cavity. This is the reason for the name of this phase. Further characteristics of this phase are shown in Figure 6b. The flow is now modestly supercritical over most of its evolution as evidenced by the F_2 profile. It also shows structure in the velocity, concentration, and especially F_2 that is synchronized to the SW structure. There is still no appreciable erosion as evidenced by $V_{\rm shr}^5$. Figure 7 shows that $m(t)$ has a maximum and remains near the initial mass. The front velocity of 0.66, 3.6 m/s in dimensional units, is not elevated or reduced. The characteristics of the deposited beds shown in Figure 5b, display a bit more structure than the previous phase. There still do not appear to be distinct beds associated with each flow. Instead there is a massive bed with gradually changing characteristics. It becomes more fine grained downslope. Vertically it shows more character that the previous phase. It gradually oscillates from bottom to top. The resulting profile has stripes of coarse grained deposits dipping down in the downslope direction.

[54] The third phase is demonstrated in Figures 5c, 6c, and 7. We call this phase "SW growth". This phase is characterized by a SW that initially grows exponentially. It is seeded from the obstacle generating a sequence of SW crests in the downstream direction. The wave then migrates slowly upstream. The obstacle is removed from the substrate by the early flows and the subsequent evolution has no memory of the initial obstacle. It should be noted that the initial substrate profile is always steep enough to support self sustainment. Further characteristics of this phase are shown in Figure 6c. The flow is significantly supercritical over the body and is marginally supercritical near the head as evidenced by the F_2 profile. It shows structure in the velocity, concentration, F_2, and erosion parameter, $V_{\rm shr}^5$ that is synchronized to the SW structure. A distinguishing characteristic of this phase is the appreciable erosion evidenced

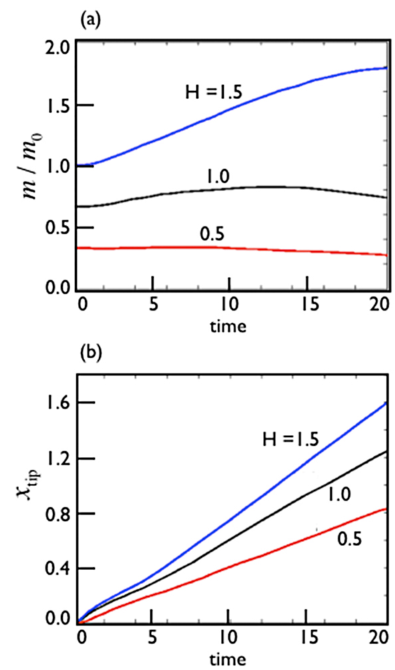

Figure 7. To study the effect of the initial height, H. (a) Normalized suspended mass in flow as a function of time, $m(t)/m_0$, for the same simulations as Figure 5 and 6: (red) "no SW," $H = 0.5$, $\theta = 0.5°$; (black) "SW buildup," $H = 1.0$, $\theta = 0.5°$; and (blue) "SW growth," $H = 1.5$, $\theta = 1.5°$. Time is plotted in normalized units (the scale for time is $t_0 = 46$ s). (b) Front position as a function of time, $x_{\rm tip}(t)$. The front velocity is reduced to 0.42 for "no SW," maintained at 0.66 for "SW buildup," and increased to 0.87 for "SW growth". In dimensional units, these are velocities of 2.3 m/s, 3.6 m/s, and 4.7 m/s.

by the V_{shr}^5 profile. It also shows a exponentially growing (from head to tail) wave structure that is synchronized to the SW structure. Figure 7 shows that $m(t)$ is monotonically increasing and approaches an asymptote that is about twice the initial mass. The front velocity of 0.87, 4.7 m/s in dimensional units, is elevated. The characteristics of the deposited beds shown in Figure 5c, are quite complex. There are distinct beds for each flow. There is an overprint of a complex structure as the SW migrate upstream and erode into the substrate.

[55] We examine the flow properties and their link to the three phases of SW formation in Figure 8. The shear velocity, V_{shr}, bottom topography, and the change in the bottom topography between consecutive flows are shown as a function of x (at normalized time t = 8). For the "no SW" phase shown in Figure 8a, the shear velocity is almost flat, the bottom topography has no undulating structure, and the change in topography between consecutive flows is very small. For the "SW buildup" phase shown in Figure 8b, the shear velocity has some structure following the variation in the topography, the bottom topography shows an undulating structure around the original obstacle, and the change in topography is very modest. For the "SW growth" phase shown in Figure 8c, the shear velocity is following the SW structure with larger values down slope and smaller values up slope, the bottom topography has an extended undulating structure, and the change in topography is oscillating between positive to negative values following the undulating structure of the shear velocity. The maxima of the change in topography is where the shear velocity a minima leading to maximum deposition. The minima of the change in topography is where the shear velocity is a maxima leading to maximum erosion. The relationship between the shear velocity and the bottom topography leads to erosion on the down slope and deposition on the upslope. This causes the SW to migrate up flow. The stream function and streamlines were also studied. No flow separation on the lee side of the SW was ever observed as predicted by *Kennedy* [1963] for Lee waves.

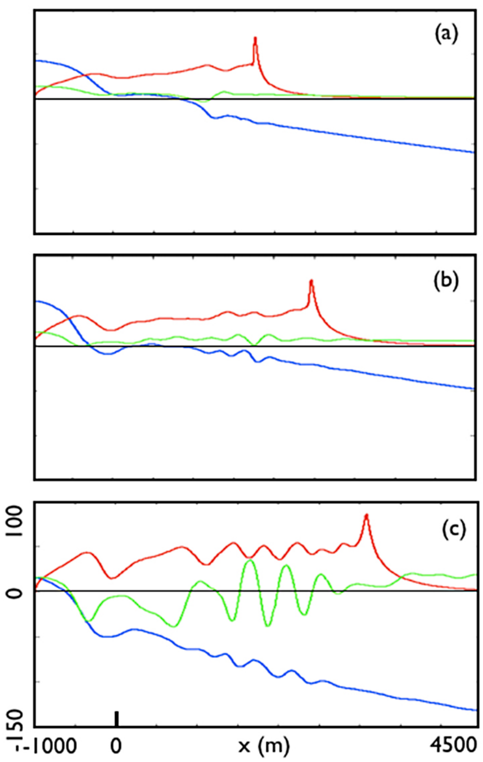

Figure 8. Flow properties and their link to the three phases of SW formation. Shown are: (red) shear velocity $V_{\mathrm{shr}} \times 500$ in m/s, (blue) bottom topography y in m, and (green) change in bottom topography $\Delta y \times 20$ in m between consecutive flows. The profiles as a function of x in m are shown for: (a) "no SW," f = 60, H = 0.5, θ_0 = 0.5°; (b) "SW buildup," f = 60, H = 1.0, θ_0 = 0.5°; and (c) "SW growth," f = 20, H = 1.5, θ_0 = 1.5°.

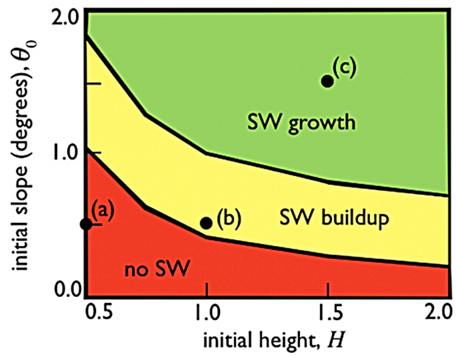

Figure 9. Phase diagram for SW in the H-θ_0 plane, where H is the initial lock height in normalized units and θ_0 is the initial slope of the substrate. The three regions are identified according to the phase of the SW: (red) "no SW," (yellow) "SW buildup," and (green) "SW growth". The points simulated in Figures 5 to 7 are plotted as black dots and labeled (a, b, and c) consistent with those figures.

[56] The picture of these phases is completed by a much larger set of simulations that were done over a large range of lock height, H, and slope angle, θ_0. For each of the simulations the flow was classified by what phase of SW developed ("no SW," "SW buildup," or "SW growth"). The results are displayed in Figure 9. This figure divides the H-θ_0 plane into three regions depending on the phase of the SW. The three exemplars shown in the previous three simulations are indicated as the black points on this figure. As H increases, θ_0 can be reduced and still maintain the SW phase. You can now see why we had to increase the angle, as well as the initial flow height, to have the third case be in the "SW growth" phase. This figure is a cut through the phase space at constant initial particle concentration, c_0, and particle size, $\{d_i\}$. The behavior of the phase diagram with these remaining two variables will be explored in the next two subsections. Three movies, one for each phase corresponding to the three substrate profiles shown in Figure 5, can be found in the auxiliary material.

[57] Before we proceed, we examine the "SW buildup" phase in a bit more detail. We described this phase as being soiliton like. A soliton is a wave with an invariant profile except that it moves at a constant velocity. Figure 10 shows this characteristic of the case shown in Figure 5b. Figure 10a shows the 5 profiles of the surface after flows 40 to 80. The profile is constant except for a lateral shift. The amount of that shift as a function of the flow is shown in Figure 10b. It displays a constant velocity of 2.3 m/flow.

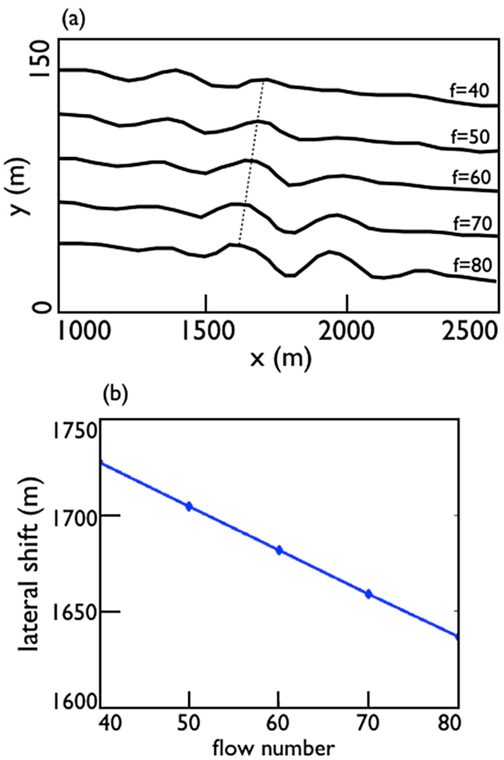

Figure 10. Soliton like behavior of the "SW buildup" phase shown in Figure 5b. (a) Profiles of the surface after flows 40 to 80. (b) Lateral shift of the constant profile as a function of the flow. It displays a constant velocity of 2.3 m/flow.

3.3. Effect of Particle Concentration

[58] We now move onto a study of the effect of initial lock concentration, c_0, on the development of the SW. With respect to the previous section, we fix the current height at H = 1.5 and study the dependance of the SW development on both c_0 and the slope angle, θ_0. It should be noted that changing c_0 has a direct effect on the system's timescale through $t_0 = L_0/u_b$, where the buoyancy velocity is $u_b = \sqrt{gR{*}c_0L_0}$. In Figure 11 the substrate structure after 80 flows is shown for three different cases, each representative of one of the phases found in the previous section. This figure is analogous to Figure 5 of the previous section.

[59] A much larger set of simulations is used to define the three regions corresponding to the phases of the SW, in a c_0-θ_0 plane (where the initial lock height, H, and particle size, $\{d_i\}$ are constants). This phase diagram is shown in Figure 12, and is analogous to Figure 9 of the previous section. Two lines divide this plane into areas of "no SW," "SW buildup," and "SW growth". As c_0 increases θ_0 can be reduced and still maintain the SW phase. The three exemplars shown in Figure 11 are indicated as black points on this figure.

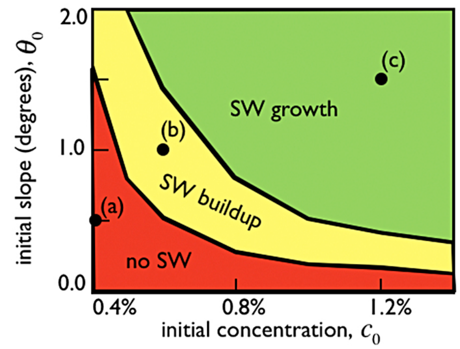

Figure 12. Phase diagram for SW in the c_0-θ_0 plane, where c_0 is the initial particle concentration and θ_0 is the initial slope of the substrate. The three regions are identified according to the phase of the SW: (red) "no SW," (yellow) "SW buildup," and (green) "SW growth". The points simulated in Figure 11 are plotted as black dots and labeled (a, b, and c) consistent with that figure.

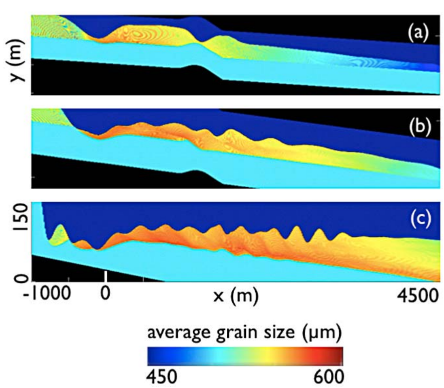

Figure 11. Development of SW on a substrate after 80 flows, to study the effect of the particle concentration, c_0. The x-y image is colored according to the average grain diameter. The initial obstacle has the reduced height shown in Figure 4. The color bar is a rainbow, starting from 450 μm at blue and ending at 600 μm at red. The profiles are shown for: (a) "no SW," c_0 = 0.4%, θ_0 = 0.5°; (b) "SW buildup," c_0 = 0.6%, θ_0 = 1.0°; and (c) "SW growth," c_0 = 1.2%, θ_0 = 1.5°.

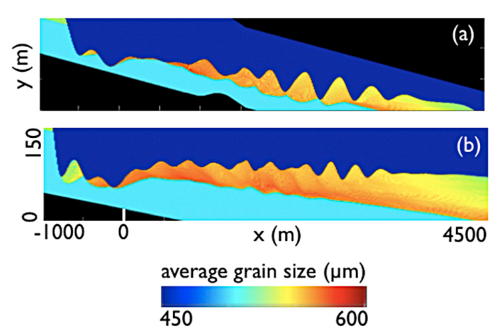

Figure 13. Development of SW on a substrate after 80 flows, to study the effect of the particle concentration, c_0, on the wavelength of the SW, λ. The x-y image is colored according to the average grain diameter. The initial obstacle has the reduced height shown in Figure 4. The color bar is a rainbow, starting from 450 μm at blue and ending at 600 μm at red. The profiles are shown for: (a) c_0 = 0.6%, θ_0 = 2.0°, where λ = 430 m and (b) c_0 = 1.2%, θ_0 = 1.5°, where λ = 310 m.

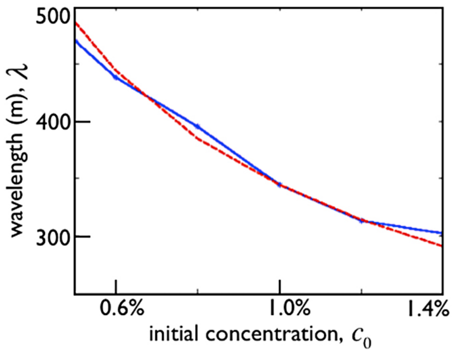

Figure 14. Dependance of SW wavelength, λ, on the initial particle concentration, c_0. The result of a set of simulations similar to those shown in Figure 13 (H = 1.5 and θ_0 = 1.5°) are shown as the blue line. A fit to the data of the form $\lambda = \lambda_1 \sqrt{c_1/c_0}$, where λ_1 = 344 m and c_1 = 1.0%, is shown as the dashed red line.

[60] A closer look is taken at the dependance of the SW wavelength, λ, by studying two "SW growth" cases with different values of c_0. These cases have c_0 values of 0.6% and 1.2%, and slope angles of 2° and 1.5°, respectively. The substrate structure after 80 flows is shown in Figure 13. Note that for the increase of c_0 by a factor of 2, the wavelength has decreased by a factor of $\sqrt{2}$ from 430 m to 310 m. This is consistent with the decrease in the timescale by a factor $\sqrt{c_0}$ with the increase of c_0. This dependance is further established by a larger set of simulations whose results are shown in Figure 14. Here the wavelength of the SW is plotted versus the initial concentration. Notice the good fit of these points to a line of the form $\lambda \propto 1/\sqrt{c_0}$. We also studied the effect on λ of variation in the other controlling variables (H, θ_0, and $\{d_i\}$). We found that there was weak or little dependance on these variables.

3.4. Dependance on Particle Diameter

[61] Finally, we turn our attention to the effect of particle diameter, d, on the development of the SW. We fix the lock height at H = 1.5, the number of grain types at one, and the initial particle concentration at c_0 = 0.8%, and study the dependance of the SW development on both d and the slope angle, θ_0. We present two cases in Figures 15 and 16, where we display the substrate structure after 25 flows. The particle diameters are 600 μm and 1000 μm (R_{pi} = 56 and 120), with

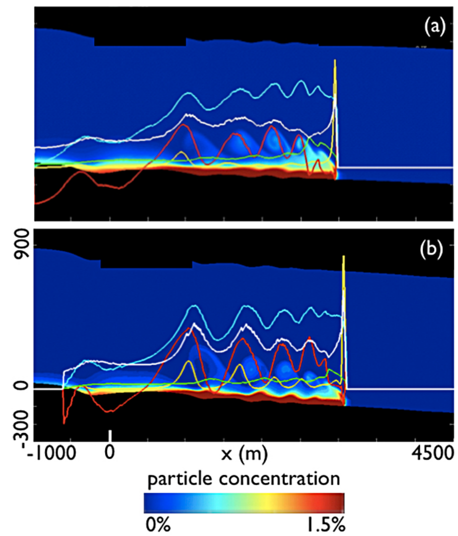

Figure 16. Particle volume concentration of the flow in the x-y plane at the normalized time, t = 8, for flow, f = 25, to study the effect of the particle diameter, d. This corresponds to simulations of Figure 15. The color bar is a rainbow, starting from 0 at blue and ending at 1.5% at red. Also shown are the depth averaged current variables: (blue) velocity $U \times 100$ in m/s, (white) concentration $C \times 2 \times 10^4$, (green) current height h in m, (red) change in Froude number $F_2 \times 200$, and (yellow) shear velocity term in the resuspension $V_{\rm shr}^5 \times 5 \times 10^6$ in (m/s)^5. All quantities plotted have SI dimensions. The profiles are shown for: (a) d = 600 μm (R_{pi} = 56), θ_0 = 1.0° and (b) d = 1000 μm (R_{pi} = 120), θ_0 = 1.5°.

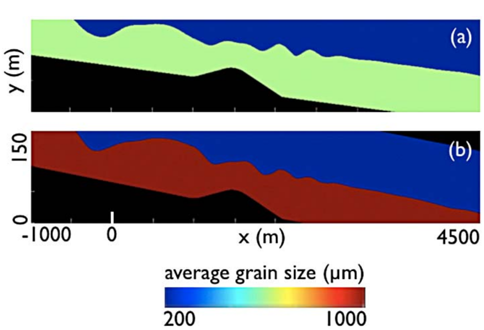

Figure 15. Development of SW on a substrate after 25 flows, to study the effect of the particle diameter, d. The x-y image is colored according to the average grain diameter. The initial obstacle has the reduced height shown in Figure 4. The color bar is a rainbow, starting from 200 μm at blue and ending at 1000 μm at red. The profiles are shown for: (a) d = 600 μm (R_{pi} = 56), θ_0 = 1.0° and (b) d = 1000 μm (R_{pi} = 120), θ_0 = 1.5°.

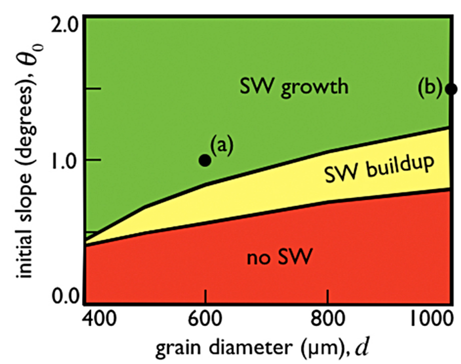

Figure 17. Phase diagram for SW in the d-θ_0 plane, where d is the particle diameter and θ_0 is the initial slope of the substrate. Range of d displayed corresponds to R_{pi} = 30 to 120. The three regions are identified according to the phase of the SW: (red) "no SW," (yellow) "SW buildup," and (green) "SW growth". The points simulated in Figure 15 are plotted as black dots and labeled (a and b) consistent with that figure.

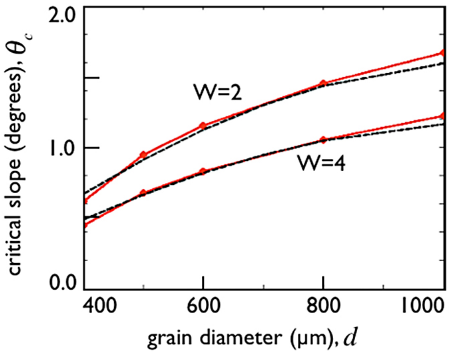

Figure 18. Critical angle for SW growth, θ_c as a function of grain diameter, d, for two different lock widths, W. The $\theta_c(d)$ curves are shown a red solid lines. A theoretical expression for the resuspension, E_s, is compared to these curves by plotting the function A/E_s, where A = 1.77 fits the W = 4 curve, and A = 2.42 fits the W = 2 curve. These fit expressions are plotted as dotted black lines.

slope angles of 1.0° and 1.5°, respectively. The two cases display a very similar development of "SW growth" to Figures 5c and 6c. As the grain diameter increases, the particle mass and the settling velocity increases, leading to more difficult resuspension. To obtain a similar SW growth for the larger grain diameter, the slope needs to be increased.

[62] A much larger set of simulations is used to define the three regions corresponding to the phases of the SW, in a d-θ_0 plane (where the initial lock height, H, and initial particle concentrations, c_0, are constants). This phase diagram is shown in Figure 17, and is analogous to Figure 12 of the previous section. Two lines divide this plane into areas of "no SW," "SW buildup," and "SW growth". The two exemplars shown in Figure 15 are indicated as black points on this figure.

[63] To establish a further connection between SW generation and resuspension, systems with two different lock widths, W, were examined—a width of 4 as in all previous simulations, and a reduced width of 2. Figure 18 shows the change in the boundary of the "SW growth" phase in the d-θ_0 plane with this decrease in W. This boundary is given by the critical angle, θ_c as a function of grain diameter, d. For this narrower lock, fewer particles are included in the current which increases the critical angle for the same diameter. The two critical angle curves, $\theta_c(d)$, are compared to the normalized inverse of the resuspension term, E_s. The Dietrich relation for the settling velocity with a characteristic normalized shear velocity of $V_{\text{shr}} = 0.15$ is used to calculate E_s. The good correlation between these curves, $\theta_c(d)$ and $E_s^{-1}(d)$, shows that SW generation is highly correlated to the resuspension mechanism.

4. Conclusions

[64] After using a high resolution 2-D computer simulation model of turbidity currents based on the Navier-Stokes equations, we have developed a better understanding of sediment wave generation. This method took into account non-linearity, used a realistic erosion model, and modeled the depth dependant behavior in a self consistent and self generating way. The geometry was a lock release of a particle laden fluid onto a slope with a small obstacle. A sufficient number of flows were simulated, the next flow started after the previous flow had completed. The obstacle is only a trigger for the sediment wave generation. After several flows, the obstacle was eroded by the resuspension and a SW was generated, characterized by the most probably wavelength, $\lambda = 2\pi h$, derived by *Normark et al.* [1980]. This is independent of any details of the initial obstacle.

[65] The feedback mechanism responsible for the generation of SW comes from an interaction of the flow with the lower boundary condition. This complex boundary condition modifies the topology of the boundary through the deposition of particles from the fluid and resuspension of particles from the substrate. The increased slope on the downstream side of an obstacle increases the kinetic energy in a flow. This will increase the resuspension, by increasing the shear in the fluid and the net effect will be increased erosion. This erosion into the substrate, creates a subsequent decrease in slope. As subsequent flows climb this decrease in slope, their kinetic energy decreases leading to increased deposition. This creates another obstacle downdip of the original one. The process then continues to generate a train of self generated and self consistent obstacles in the downstream direction. This self consistent train of obstacles is the SW.

[66] There is an upward migration of the SW caused by another feedback mechanism. Once the SW is established, the flow will preferentially deposit on the parts of the wave with increased slope and preferentially erode the parts of the wave with decreased slope. The result will be a migration of the wave updip.

[67] Conditions are not always favorable for having this feedback. We found that there are four system parameters that influence the sediment wave growth: (1) slope, θ_0; (2) current lock height, H; (3) grain lock concentration, c_0; and (4) particle diameters, $\{d_i\}$. The behavior of the system was studied over a range of these parameters, $0° \le \theta \le 2°$, $0 < H \le 2$, $0.4\% \le c_0 \le 1.2\%$, $400\ \mu\text{m} \le d \le 1000\ \mu\text{m}$, and up to 120 flows. Three phases of the system were found: (1) "no SW," (2) "SW buildup," and (3) "SW growth". These phases are characterized by whether or not the conditions are favorable for the feedback which leads to SW growth. For the first phase, the conditions are always unfavorable. For the second phase, the conditions are sometimes favorable (on the downslope side of the obstacle). For the third phase, they are always favorable. The conditions are determined by the parameters. This allowed us to do systematic parameter studies and define three regions in the four dimensional (θ_0, H, c_0, d) space according to the phase of the system – the phase diagram.

[68] It should be noted why we only considered the four variables (θ_0, H, c_0, d). An analysis of dimensionless partial differential equations (6)–(8) for ω, ψ and $\{c_i\}$ indicates that there should be three governing parameters associated with the gravity unit vector, $\hat{g}$, typical vorticity, ω_0, and the average settling velocity, $\langle u_{si} \rangle$. Here we have reduced the set of particle concentration equations, over index i, to only one for the total concentration, c. We have neglected first order, Δd (sorting), and higher order effects on the substrate phase. The dependance on R_e and P_e have been neglected because

of the reasons stated in section 2.3. Although the dependance on c_0 is normalized out of these equations, it is reintroduced by the resuspension in equation (13). We now have four governing parameters. The average $\langle u_{si} \rangle$ can be associated with the particle size d, $\hat{g}$ can be associated with θ_0, the resuspension with c_0, and finally ω_0 can be associated with H. The lock height, H, is really a surrogate for the flow size. Little dependance was found to the aspect ratio, W/H, of the lock by *Blanchette et al.* [2005] and by us when the lock width was doubled, and the dependance on the lock width, W, can be normalized out of the problem by L_o. We now see that the four governing parameters can be associated with the four variables that were studied.

[69] Each phase was found to be characterized by several different things. The first and most simple phase, "no SW," has a simple structure. There in no development of SW or periodic structures in the flow. The flow has a monotonically decreasing mass as a function of time. There is no significant erosion. The deposited substrate has little evidence of the individual flows. It appears to have one massive bed that becomes gradually more fine grained downslope and gradually more coarse grained from bottom to top. The second phase, "SW buildup," has some more structure. There is a rather rapid local development of a SW, but this SW then reaches a steady state profile. The flow, as a function of time, has a relatively constant mass with a maximum. It shows a periodic structure in velocity, concentration and especially F_2 that correlates to the SW wave structure. There is no appreciable erosion. The deposited substrate still has little evidence of the individual flows. It has one massive bed with gradually changing characteristics. It becomes more fine grained downslope. Vertically is shows more character than the first phase with the grain size showing an gradually oscillatory behavior. The third phase, "SW growth," has significant structure. There is a global development of a SW that initially grows exponentially. The flow has a monotonically increasing mass that nearly doubles. It shows structure in the velocity, concentration, F_2, and erosion that are synchronized to the SW structure. It has significant erosion that increases exponentially in the upstream direction within the flow. The deposited substrate has distinct deposited beds for each flow that show a complex structure.

[70] We found that the driving force behind the establishment of the SW is the self sustainment of the flow. This is evidenced by the time evolution of the mass, the threshold for the SW generation, boundaries of the SW phases, and the functional dependance of the critical angle, $\theta_0(d)$, for various initial lock widths.

[71] The wavelength of the SW, λ, was found to be a significant function of the grain lock concentration, c_0. It scaled as $1/\sqrt{c_0}$, directly related to how the timescales. The three other system parameters were found to have weak or little effect on λ.

[72] SW generation presented in the linear stability analysis (LSA) [*Flood*, 1988; *Lesshafft et al.*, 2011] is of a different physical origin than the one presented in this study. In the LSA, internal waves (Lee waves) are generated in the basal boundary layer, the shear layer, of the stratified flow as it passes over an undulating erodible bed. These internal waves generate a coherent coupling with the bottom topography and can be a mechanism for unstable growth of SWs. In our nonlinear study, the SW is coupled to the lower and upper parts of the current, simultaneously. In our case, SWs are generated by erosion and deposition from a single obstacle and this induces the most probable wavelength for the growing SW. In the LSA, a key condition for an unstable wave to occur is that the flow velocity thickness of the boundary layer needs to be thinner than the concentration thickness of the boundary layer; while the flow can be sub or super critical. In our case the current needs to be self sustaining, with erosion larger than deposition, or super critical over a wide spatial range in the x direction. In the LSA, the unstable SW wavelength is typically in the range of 1–10 km. In our case, the wavelength is relatively shorter and is consistent with the relation $\lambda = 2\pi h$. For current height, h, in the range 50 to 100 m, the wavelength, λ, is in the range 300 to 600 m. In LSA and in our case, the growing SW tend to migrate upslope, by depositing during the up-flow and eroding during the down-flow; this is consistent with field observation. We conclude that LSA and our study give two different physical origins for SW generation: SW in LSA, are generated in basal boundary layer of the flow and have a relatively longer wavelength; and SW, in our case, are correlated with the bulk flow and have a relatively shorter wavelength.

[73] Finally, we discovered a rather direct path from the physics of the flow to the structure of the deposited substrate. Starting with the flow, the work of *Blanchette et al.* [2005] established two regimes depending on whether the flow is self sustaining or depositing. Our work has established the relationship between self sustainment within one flow and sediment wave generation on the substrate surface over multiple flows. In fact, there are phases of SW formation, determined by whether the system never, sometimes or always generates SW. The phase is determined by four system parameters, and a phase diagram can be constructed in terms of these parameters. There are strong indications that there is a further direct relationship between the phase of SW formation and the structure of the deposited substrate. This structure can be identified as a geologic texture, or more commonly called geologic facies. This is a very remarkable result – there are physical phases that could well correspond to geologic facies.

[74] Future work will focus on further study on the emergent structure appearing in the deposited substrate. Longer runs are needed to see the stationary character of the self organization, and modern techniques might be used to characterize the self organization. We are also interested in understanding the effect of the sorting, Δd, on the substrate phase diagram. Three issues need to be refined to have more realistic models and quantitative results. In 2-D, the influence of larger $R_e > 1000$ on the phase diagram of SW generations needs to be simulated and studied. A closure relation for the turbidity current dynamics, which depends on the turbulent energy, is required. 3-D simulation would be useful in obtaining a consistent shear layer that includes the turbulent structure. This could be applied to construct the shear velocity from basic principles for the 2-D simulation. Detailed, first principles, simulations of the grain-fluid interactions, in both 2-D and 3-D, would be very useful in deriving a resuspension model from basic principles that can be included in the 2-D simulation.

[75] **Acknowledgments.** The authors thank Eckart Meiburg, Ben Kneller and Francois Blanchette for many useful discussions. Large parts of the computer code used in this research were developed by Eckart Meiburg and his group at UCSB. We also are grateful to Stanislav Kuzmin for his help in developing the parallel computer code we used in the work and for his many useful technical interactions. This work was supported by the CSIRO Office of the Chief Executive Science Fund. Calculations were done using the CSIRO GPU Cluster with significant assistance from Ondrej Hlinka.

References

Ablowitz, M. J., and H. Segur (1984), *Solitons and the Inverse Scattering Transform*, Soc. for Ind. and Appl. Math., Philadelphia, Pa.

Arecchi, F. T., W. Gadomski, R. Meucci, and J. A. Roversi (1989), The dynamics of laser buildup from quantum noise, *Phys. Rev. A*, *39*, 4004–4015.

Blanchette, F., M. Strauss, E. Meiburg, B. Kneller, and M. E. Glinsky (2005), High-resolution numerical simulations of resuspending gravity currents: Conditions for self-sustainment, *J. Geophys. Res.*, *110*, C12022, doi:10.1029/2005JC002927.

Blanchette, F., V. Piche, E. Meiburg, and M. Strauss (2006), Evaluation of a simplified approach for simulating gravity currents over slopes of varying angles, *Comput. Fluids*, *35*, 492–500.

Cantero, M. I., J. R. Lee, S. Balachandar, and M. H. Garcia (2007), On the front velocity of gravity currents, *J. Fluid Mech.*, *586*, 1–39.

Cantero, M. I., S. Balachandar, M. H. Garcia, and D. Bock (2008), Turbulent structure in planar gravity currents and their influence on the flow dynamics, *J. Geophys. Res.*, *113*, C08018, doi:10.1029/2007JC004645.

Choi, S., and M. H. Garcia (2002), κ–ϵ Turbulence modeling of density currents developing two dimensionally on a slope, *J. Hydral. Eng.*, *128*, 55–63.

de Roojj, F., and S. B. Dalziel (2001), Time- and space-resolved measurements of deposition under turbidity currents, *Spec. Publ. Int. Assoc. Sedimentol.*, *31*, 207–215.

Dietrich, W. E. (1982), Settling velocity of natural particles, *Water Resour. Res.*, *18*, 1615–1626.

Druzhinin, O. A. (1995), On the two-way interaction in two-dimensional particle-laden flows: The accumulation of particles and flow modification, *J. Fluid Mech.*, *297*, 49–76.

Felix, M. (2001), A two-dimensional numerical model for turbidity currents, *Spec. Publ. Int. Assoc. Sedimentol.*, *31*, 71–81.

Fildani, A., W. R. Normark, S. Kostic, and G. Parker (2006), Channel formation by flow-stripping: Large-scale scour features along the monterey east channel and their relation to sediment waves, *Sedimentology*, *53*, 1265–1287.

Flood, R. D. (1988), A lee wave model for deep-sea mud wave activity, *Deep-Sea Res.*, *35*, 973–983.

Garcia, M. H., and G. Parker (1993), Experiments on the entrainment of sediment into resuspension by a dense bottom current, *J. Geophys. Res.*, *98*, 4793–4807.

Hall, B. (2009), Submarine channel and sediment wave formation by turbidity currents: Navier-stokes based linear stability analysis, Ph.D. thesis, Univ. of Calif. Santa Barbara, Santa Barbara.

Hall, B., E. Meiburg, and B. Kneller (2008), Channel formation by turbidity currents: Navier-Stokes based linear stability analysis, *J. Fluid Mech.*, *615*, 185–210.

Hartel, C., E. Meiburg, and F. Necker (2000), Analysis and direct numberical simulation of the flow at a gravity current head, part 1: Flow topology and front speed for slip and no-slip boundaries, *J. Fluid Mech.*, *418*, 189–212.

Huang, H., J. Imran, and C. Pirmez (2000), Numerical study of turbidity currents with sudden-release and sustained-inflow mechanisms, *J. Hydraul. Eng.*, *134*, 621–653.

Huppert, H. E., and J. E. Simpson (1980), The slumping of gravity currents, *J. Fluid Mech.*, *99*, 785–799.

Kennedy, J. F. (1963), The mechanics of dunes and antidunes in erodible-bed channels, *J. Fluid Mech.*, *16*, 521–544.

Kostic, S., and G. Parker (2006), The response of turbidity currents to a canyon-fan transition: Internal hydraulic jumps and depositional signatures, *J. Hydraul. Res.*, *44*, 631–653.

Kubo, Y., and T. Nakajima (2002), Laboratory experiments and numerical studies of sediment-wave formation by turbidity currents, *Mar. Geol.*, *192*, 105–121.

Lee, H. J., J. P. M. Syvitski, G. Parker, D. Orange, J. Locat, E. W. H. Hutton, and J. Imran (2002), Distinguished sediment waves from slope failure deposits: Field example, including the humboldt slide, and modeling results, *Mar. Geol.*, *192*, 79–104.

Lele, S. K. (1992), Compact finite difference schemes with spectral-like resolution, *J. Comp. Phys.*, *103*, 16–42.

Lesshafft, L., B. Hall, E. Meiburg, and B. Kneller (2011), Deep-water sediment wave formation: Linear stability analysis of coupled flow/bed interaction, *J. Fluid Mech.*, *680*, 435–458.

Meiburg, E., and B. Kneller (2010), Turbidity currents and their deposits, *Ann. Rev. Fluid Mech.*, *42*, 135–156.

Middleton, G. V. (1993), Sediment deposition from turbidity currents, *Earth Planet Sci.*, *21*, 89–114.

Necker, F., C. Hartel, L. Kleiser, and E. Meiburg (2002), High-resolution simulations of particle-driven gravity currents, *Int. J. Multiphase Flow*, *28*, 279–300.

Normark, W. R., G. R. Hess, D. A. V. Stow, and A. J. Bowen (1980), Sediment waves on the monterey fan levee: A preliminary physical interpretation, *Mar. Geol.*, *37*, 1–18.

Pantin, H. M., and M. C. Franklin (2009), Predicting autosuspension in steady trubidity fow: Ignition point and their relation to richardson numbers, *J. Sediment. Res.*, *79*, 862–871.

Parker, G., and N. Izumi (2000), Purely erosional cyclic and solitary steps created by flow over a cohesive bed, *J. Fluid Mech.*, *419*, 203–238.

Parker, G., Y. Fukushima, and H. M. Pantin (1986), Self-accelerating turbidity currents, *J. Fluid Mech.*, *171*, 145–181.

Parker, G., C. Parola, and S. Leclair (2000), Probabilistic exner sediment continuity equation for mixtures with no active layer, *J. Hydraul. Eng.*, *126*, 818.

Pratson, L. F., J. Imran, E. W. H. Hutton, G. Parker, and J. P. M. Syvitski (2001), BANG1D: A one-dimensional Lagrangian model of subaqueous turbid surges, *Comput. Geosci.*, *27*, 701–716.

Sequeiros, O. E., H. Naruse, N. Endo, M. H. Garcia, and G. Parker (2009), Experimental study on self-accelerating turbidity currents, *J. Geophys. Res.*, *114*, C05025, doi:10.1029/2008JC005149.

Sun, T., and G. Parker (2005), Transportational cyclic steps created by flow over an erodible bed. Part 2. Theory and numerical simulations, *J. Hydraul. Res.*, *43*, 502–514.

Taki, K., and G. Parker (2005), Transportational cyclic steps created by flow over an erodible bed. Part 1. Experiments, *J. Hydraul. Res.*, *43*, 488–501.

Wright, S., and G. Parker (2004), Flow resistance and suspended load in sand-bed rivers: Simplified strification model, *J. Hydraul. Eng.*, *130*, 796–805.

Wynn, R. B., and D. A. V. Stow (2002), Classification and characterization of deepwater sediment waves, *Mar. Geol.*, *192*, 7–22.

Wynn, R. B., P. P. E. Weaver, G. Ercilla, D. A. V. Stow, and D. G. Masson (2000), Sedimentary processes in the selvage sediment-wave field, NE Atlantic: New insights into the formation of sediment waves by turbidity currents, *Sedimentology*, *47*, 1181–1197.